Wannier-function based scattering-matrix formalism for photonic crystal circuitry

Daniel Hermann,[1,*] Matthias Schillinger,[1] Sergei F. Mingaleev,[1,2] and Kurt Busch[1,3]

[1]*Institut für Theoretische Festkörperphysik, Universität Karlsruhe, 76128 Karlsruhe, Germany*
[2]*Bogolyubov Institute for Theoretical Physics of the National Academy of Sciences of Ukraine, 03680 Kiev, Ukraine*
[3]*Department of Physics and College of Optics and Photonics: CREOL and FPCE, University of Central Florida, Orlando, Florida 32816, USA*
[*]*Corresponding author: hermann@tfp.uni-karlsruhe.de*

Received September 10, 2007; accepted November 19, 2007;
posted December 20, 2007 (Doc. ID 87373); published January 29, 2008

A guided-mode scattering matrix approach to photonic crystal integrated devices, based on the expansion of the electromagnetic field in Wannier functions is presented and its applicability to large-scale photonic circuits is demonstrated. In particular, we design two components typically used in wavelength division multi/demultiplexing applications, namely, a directional coupler and a Mach–Zehnder interferometer, and we analyze the transmission spectra as a function of the coupler length and/or delay line length, respectively. These examples demonstrate that by cascading basic functional elements, large-scale circuits can be accurately described and efficiently designed with minimal numerical effort. © 2008 Optical Society of America

OCIS codes: 230.5298, 230.3120, 350.4238.

1. INTRODUCTION

Photonic crystals (PhCs) [1], periodic nanostructured dielectric materials with periodicities on the order of the wavelength of light, are ideal candidates for integrated all-optical devices. By introducing line defects, waveguides can be created within the photonic bandgap of the underlying PhCs. Furthermore, in contrast to index-guided optical elements, light can be guided around sharp bends [2] over broad frequency ranges, due to the vanishing photonic density of states in the surrounding PhC.

Over the past decade, extensive studies have been carried out about different types of basic functional elements (FEs) built into 2D PhCs. The potential for broadband single-mode waveguides [3] and bends [4,5], as well as for more complex devices, such as directional couplers (DCs) [6,7] and Mach–Zehnder interferometers (MZIs) [8,9], has been demonstrated. In addition, various concepts for active tunability have been proposed [10–13].

Although many of these studies have been targeted at characterizing defect structures in the very specific environment of a 2D PhC, most calculations were done using all-purpose techniques, such as the finite-difference time-domain (FDTD) method, finite element methods, or beam propagation methods. While these methods are very powerful for structures with an arbitrary distribution of dielectric material, they lose some efficiency in highly ordered structures such as PhCs, since they do not exploit the symmetry properties and band structure of the underlying PhC. Furthermore, the simulation of large-scale devices is very memory and/or time consuming, especially in the case when slow light regimes [8] are involved in one of the components.

In this paper, we propose a guided-mode scattering-matrix approach for the efficient treatment of PhC circuits and demonstrate its applicability to large-scale circuits. The approach extends the concepts presented in [14]; it relies on the efficient calculation of the scattering matrices (S-matrices) of certain basic FEs of a circuit such as bends or coupler end points via the Wannier-function technique [15]. Each S-matrix contains amplitude and phase information of how the corresponding FE relates waveguiding modes in the different device ports to each other. Therefore, similar to impedance matrices in microwave engineering, the circuit S-matrix of a complex device can then be computed through the combination of S-matrices of the basic FEs. As a result, this approach scales favorably with circuit size.

2. MODEL SYSTEM

To be specific, we consider a 2D macroporous silicon PhC host material (refractive index $n=3.46$) with pores of radius $r=0.45a$ arranged on a triangular lattice (lattice constant a) [16]. For H-polarized radiation, i.e., when light with the magnetic field polarized along the pore axis propagates in the plane of periodicity, this system exhibits a large bandgap ($\Delta\omega/\omega_c=49\%$ relative to the center gap frequency ω_c) in the frequency range $\omega a/2\pi c \equiv a/\lambda = [0.298, 0.490]$. FEs may be created by infiltrating single pores with low-index materials such as polymers or liquid crystals with typical refractive indices in the range of $n = 1.5, \ldots, 1.7$ [17].

For instance, a single-mode waveguide in the frequency range $a/\lambda=[0.357, 0.407]$ with a bandwidth of $\Delta\omega/\omega_c = 13\%$ can be created by filling a row of pores with a polymer of refractive index $n=1.7$. In Fig. 1, we compare the resulting waveguide dispersion relations computed within the Wannier-function approach with supercell calculations based on a plane wave expansion [18]. Very good

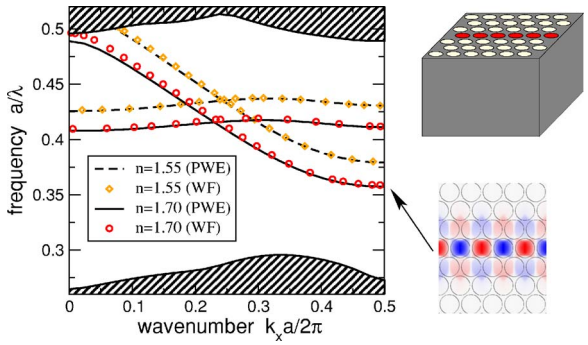

Fig. 1. (Color online) Model system: 2D macroporous silicon PhC with pores of $r=0.45a$ arranged on a triangular lattice. A large bandgap ($\Delta\omega/\omega_c=49\%$) exists for H-polarized light. Within the gap, the waveguide dispersion is shown for a line of pores filled with a low-index material of refractive index n. The dispersion calculated with the Wannier-function technique (WF; symbols) is compared with results from plane-wave based supercell calculations (PWE; curves). We are mostly interested in the single-mode frequency range below the cutoff frequency of the almost flat dispersion branch, i.e., $a/\lambda=[0.357,0.407]$ for $n=1.7$. The corresponding propagating waveguide mode exhibits even symmetry (lower right panel).

agreement between the two methods is found except for frequencies close to the upper band edge. There, the waveguide modes become very extended in the lateral direction so that the plane wave expansion (PWE) calculations for the resulting very large unit cells become less reliable.

3. SCATTERING-MATRIX FORMALISM

A photonic circuit consists of a number of waveguide ports for incoming and outgoing signals and is fully characterized by its S-matrix, which relates amplitudes and phases of incoming to outgoing guided modes in the waveguide ports. The S-matrix contains all relevant information about the reflectances and transmittances as well as the phase relations between mode amplitudes in the different ports.

The direct computation of a large-scale circuit S-matrix is numerically expensive if not impractical due to the large system size. The basic idea behind the S-matrix approach is to split a large circuit into certain basic FEs, such as bends, and to interconnect them via waveguides of variable lengths. This principle is depicted in Fig. 2. The S-matrices of the individual FEs can be computed with much less effort as compared to the full circuit S-matrix. Once they are obtained, the full S-matrix of the entire circuit is easily calculated for any lengths of the waveguides connecting the individual basic FEs. Thus, length-dependent characteristics of the circuit can be easily computed. This provides a very powerful design tool for PhC circuits. At this point, we would like to note that the guided-mode S-matrix approach has been developed and is widely used in high-frequency electrical engineering to characterize and design microwave circuits [19].

A. Scattering Matrix of Individual Functional Elements

The wave equation for H-polarized fields in 2D systems reads

$$\left[\nabla_2\cdot\frac{1}{\epsilon(\vec{r})}\nabla_2+\frac{\omega^2}{c^2}\right]H_z(\vec{r})=0, \tag{1}$$

where $\nabla_2\equiv(\partial_x,\partial_y)$ is the gradient in the 2D plane. To solve Eq. (1) for defect structures in PhCs, we expand the magnetic field H_z into Wannier functions [15]. This localized function basis is derived from the Bloch modes of the underlying PhC by a lattice Fourier transform. Therefore, the Wannier-function basis contains all information about symmetries and bandgaps of the PhC; it is orthonormal by construction, and it acquires certain translational properties. For instance, the Wannier function $W_{n\vec{R}}(\vec{r})$, labeled by lattice vector $\vec{R}$ and band index n, is identical to the Wannier function $W_{n\vec{0}}(\vec{r}-\vec{R})$, which is centered at the unit cell around the origin and has been shifted by $\vec{R}$. These properties make the Wannier basis ideally suited to describe localized defect modes in the perturbed PhC.

In Fig. 3, we display the 26 maximally localized photonic Wannier functions that have been employed in order to achieve converged results in all computations displayed in this paper (cf. Fig. 1 for a quantitative comparison of waveguide dispersion relations with plane-wave based supercell calculations). To the best of our knowledge, these Wannier functions represent the first maximally localized and PhC-symmetry compliant Wannier functions for H-polarized radiation for groups of nonisolated (entangled) bands. Details about their generation can be found in [20].

To simplify the notation, we introduce a composite index $\beta=\{n,\vec{R}\}$ that labels the Wannier functions. The expansion $H_z(\vec{r})=\Sigma_\beta H_\beta W_\beta(\vec{r})$ inserted into Eq. (1) leads to the system of equations

$$\sum_\beta M_{\alpha\beta}(\omega)H_\beta=0. \tag{2}$$

The matrix $M_{\alpha\beta}(\omega)$ contains frequency-independent overlap matrix elements of the Wannier functions with respect to the full dielectric function $\epsilon(\vec{r})=\epsilon_p(\vec{r})+\delta\epsilon(\vec{r})$, thus including contributions mediated by the unperturbed PhC, $\epsilon_p(\vec{r})$, and the deviation from periodicity brought about by the FE, $\delta\epsilon(\vec{r})$ (see [15] for more details). The frequency enters these equations as a parameter only.

Any functional element is divided into two regions: the waveguiding region, Ω_W (union of all port regions), where the field can be described by incoming and outgoing guided modes $G_l^{\text{in/out}}(\vec{r})=\Sigma_\beta G_{\beta l}^{\text{in/out}}W_\beta(\vec{r})$ ($l=1,\ldots,N_l$), and

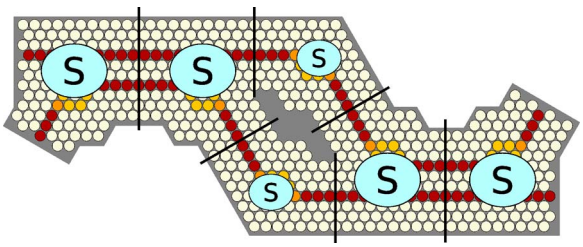

Fig. 2. (Color online) Principle of the S-matrix formalism: a large-scale circuit is divided into basic FEs that are each described by their individual S-matrices. Typically, the same FEs appear multiple times in different orientations, and their S-matrices can be reused. The complex MZI circuit depicted above is composed of only two basic FEs.

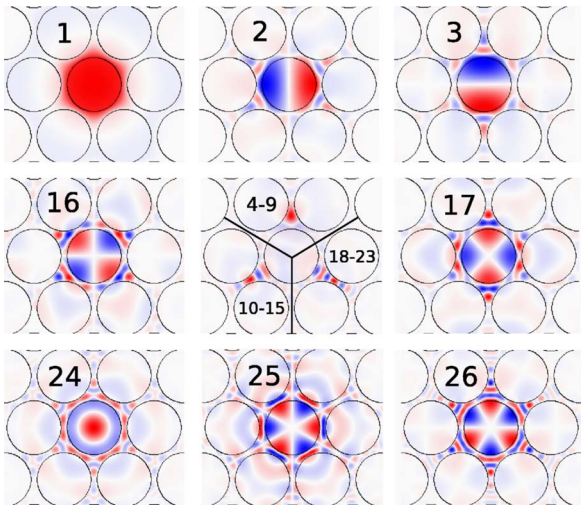

Fig. 3. (Color online) Maximally localized photonic Wannier functions related to the 26 lowest bands of the model system. Each Wannier function is labeled by its band index n. The Wannier functions associated with bands 4–9, 10–15, and 18–23 can, respectively, be obtained from the three representative functions shown in the center of the figure through five successive 60° rotations. For instance, the set of Wannier functions 4–9 forms a sixfold star, where each spike of the star is identical to the (suitably rotated) Wannier function shown. For the parameters of the model system, we refer to Fig. 1.

the central region of the device, Ω_D, where the scattering of incoming into outgoing modes takes place (see Fig. 4). The guided modes in the waveguiding region Ω_W can either be propagating or evanescently decaying into or away from the device. They are consecutively labeled over all waveguides. Thus, in the case of equal ports, each of them having n_l incoming and n_l outgoing modes, the guided modes in port 1 that propagate or grow into the same direction are indexed by $l=1,\ldots,n_l$, those in port 2 by $l=n_l+1,\ldots,2n_l$, and so on, with $N_l=N_{\text{ports}}\cdot n_l$. This compact notation avoids an additional notational overhead related to summations over the ports of the FE.

The S-matrix relates the incoming modes with mode amplitudes a_l to the outgoing modes with mode amplitudes b_l. Therefore, in Eq. (2), we replace the unknowns H_β in the waveguide region Ω_W with these guided-mode amplitudes, a_l and b_l. Next, we separate the contributions involving incoming amplitudes a_l from those involving outgoing amplitudes b_l and the central region Wannier coefficients H_β, and move them on the right hand side of the system of equations,

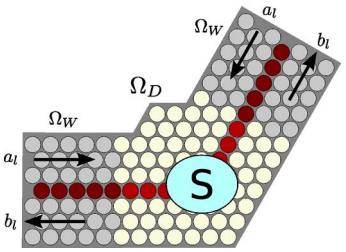

Fig. 4. (Color online) Division of a given FE into two regions, Ω_D and Ω_W. In the waveguiding region, Ω_W (shaded), the electromagnetic field can be described by incoming and outgoing guided modes and, therefore, the Wannier coefficients H_β can be replaced by guided mode amplitudes, a_l (incoming) and b_l (outgoing), in that region.

$$\sum_{\beta\in\Omega_D} M_{\alpha\beta}H_\beta + \sum_{\beta\in\Omega_W} M_{\alpha\beta}\sum_{l=1}^{N_l} G_{\beta l}^{\text{out}} b_l = -\sum_{\beta\in\Omega_W} M_{\alpha\beta}\sum_{l=1}^{N_l} G_{\beta l}^{\text{in}} a_l. \tag{3}$$

Finally, by choosing the incoming field amplitudes $a_l=\delta_{lj}$ with an arbitrary but fixed value $j\in[1,N_l]$, and solving Eq. (3) for the corresponding outgoing field amplitudes b_l, we obtain one column of the S-matrix, $S_{lj}=b_l$. The full S-matrix is computed by repeatedly solving Eq. (3) for all incoming field conditions $j=1,\ldots,N_l$.

B. Reduced Scattering Matrix

The waveguides connected to the ports of an FE usually support only a few propagating guided modes; the vast majority of guided modes is evanescent. These evanescent modes play an important role in the near field of structures that break the translational symmetry of the waveguide. In addition, they are necessary to correctly describe field components that evanescently decay away from defect structures. Therefore, we have to take them into account when computing the S-matrices of individual FEs.

On the other hand, outgoing evanescent field components die out very rapidly away from the FE and, therefore, have only negligible overlap with fields in a neighboring FE, once the FEs are sufficiently far separated. For the computation of the circuit S-matrix, it is, therefore, possible to work with reduced S matrices of individual FEs, in which only the propagating modes are retained after the S-matrix has been computed with the help of all modes (see also [14] for a detailed discussion of this issue with an illustrative example). For instance, for the waveguide bend shown in Fig. 6, i.e., for two-port FEs with single-mode waveguide ports, the reduced S-matrix is a 2×2-matrix. Similarly, for the coupler end point shown in Fig. 7, i.e., a three-port device with two single-mode waveguide ports and one dual-mode waveguide port, the reduced S-matrix is a 4×4 matrix.

C. Congruence of Functional Elements

The S-matrix of an FE depends on the position of the ports and the scatterers in the FE relative to each other, but it does not depend on the orientation of the FE as a whole (including ports) within the background PhC. For instance, the bend shown in Fig. 6 exhibits the same S-matrix as a bend that is rotated by 60°.

In general, we can say that all FEs that are congruent (i.e., that can be transformed into each other by translations, rotations, and mirror reflections) possess the same S-matrix, provided that the guided modes in the ports of two congruent FEs are mapped exactly onto each other by the congruence transformation. In our model system, the single propagating guided mode in the single-mode waveguide is even under a mirror reflection at the plane along the line defect (see Fig. 1) and is mapped onto itself for any possible congruence transformation of the bend in Fig. 6. Therefore, all congruent bends have the same S-matrix.

The situation is similar for the coupler end point shown in Fig. 7. However, the mapping of the guided modes in the dual-mode waveguide (port 3) is more complex, i.e.,

the two guided modes may be swapped by certain congruence transformations (for instance by a glide reflection at the central axis of the dual-mode waveguide). Therefore, the S-matrices of two congruent coupler end points may differ in the ordering of rows and columns.

Nevertheless, by carefully taking into account the above symmetry considerations, we can save a major amount of computations when analyzing a complex circuit such as the MZI depicted in Fig. 2. The two basic FEs that constitute this circuit, i.e., the waveguide bend and the coupler end point, have to be calculated only for one specific orientation. The S-matrices for all other orientations can then be derived according to the congruence rules described above. Therefore, in this specific example, four out of six S-matrix computations can be saved. In addition, we would like to note that a comparison of the S-matrices for simple FEs that have been obtained numerically for two equivalent orientations provides a very stringent test on the quality of the Wannier functions used in the calculations.

D. Scattering-Matrix Combination

Each individual FE has a number of ports, where each port exhibits a certain number of channels, i.e., modes supported by the corresponding waveguide. When connecting two FEs, the resulting combined FE inherits the "exterior" ports of the two FEs, i.e., the ports that are not involved in the connection. The "interior" ports, i.e., those ports that are part of the connection between the individual FEs, are eliminated in such a way that the coupling of the two FEs is correctly accounted for in the combined S-matrix. Figure 5 illustrates the general procedure of combining S-matrices of different FEs. The combined S-matrix is calculated after the scheme

$$S_{\text{combined}} = S_{\text{e,e}} + S_{\text{e,i}}(T - S_{\text{i,i}})^{-1} S_{\text{i,e}}. \tag{4}$$

Here, the S-matrices on the right hand side are assembled from blocks of the S-matrices S and S' of the individual FEs. We have introduced composite symbolic indices, "e" for exterior and "i" for interior ports. For instance, $S_{\text{e,i}}$ includes all entries of S and S' that connect incoming modes in interior ports with outgoing modes in exterior ports. In the example in Fig. 5, these are the submatrices S_{14}, S_{24}, S_{34}, $S'_{1'2'}$, and $S'_{3'2'}$. $S_{\text{e,e}}$, $S_{\text{i,i}}$, and $S_{\text{i,e}}$ are constructed similarly from blocks of S and S' that connect incoming/outgoing modes in interior/exterior ports, respectively. The switching matrix T contains all information about the guided-mode mismatch at the interior ports and the phase shifts due to a certain length of the waveguide section that connects the two devices. In the simplest situation when there is no mode mismatch at the interior ports of the two devices, i.e., when the connecting waveguide fits to both interior ports, the switching matrix T takes the form of a reflectionless S-matrix and contains only exponentials of the guided-modes' phase shifts over the length of the waveguide. The DC in Fig. 8 is an example for the simplest case of two connected FEs with no mismatch at the interior ports.

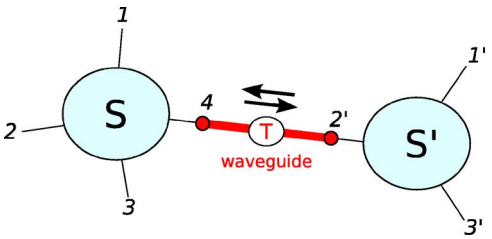

Fig. 5. (Color online) Illustration of how to connect two individual FEs with S-matrices S and S' to form a more complex FE. The interior ports 4 and 2′ are eliminated, while the exterior ports 1, 2, 3, 1′, and 3′ form the new ports of the combined FE. The length of the waveguide connecting the two FEs appears as a phase factor in the switching matrix T. In addition, the switching matrix accounts for the potential mode mismatch in the case of when waveguides at ports 4 and 2′ are different.

As alluded to above, for sufficiently well separated FEs, only the S-matrix blocks for propagating modes are taken into account. As a result, the individual S-matrices are very small (2×2 for the waveguide bend and 4×4 for the coupler end point in our case), so that Eq. (4) can be evaluated with minimal effort.

Finally, the successive application of this scheme to all connections in a circuit allows the computation of the circuit's full S-matrix. Thus, large-scale circuits can be built up easily, as soon as all S-matrices of the basic building blocks have been determined. Adding one more FE to an existing circuit requires only one additional application of Eq. (4).

4. BASIC FUNCTIONAL ELEMENTS

For the DC and MZI circuits presented in Section 5, we require only three basic FEs: the waveguide bend, the coupler end point, and the delay line transition. Below, we discuss each of them in detail.

A. Waveguide Bend

This functional element occurs in almost every circuit. It is essential for the performance of the circuit to avoid internal reflections, which compromise or even destroy the functionality of the circuit. Therefore, we optimize the simple bend so that it has minimal reflection over a given frequency range under the given design degrees of freedom (Fig. 6). The optimization procedure is analogous to that employed in [21,22] for different devices in the case of E-polarized light. In the present case, we allow a set of 3×3 pores in the bend region that are either unfilled or filled with a low-index material with variable refractive index.

B. Coupler End Point

The directional coupler described in Subsection 5.A can be split into two equivalent end points that are connected over a coupling section with two parallel waveguides (see Fig. 8). The coupler end point (Fig. 7) is the region where the two waveguides (ports 1 and 2) approach each other and end up parallel to form the coupling section (port 3, multimode waveguide). The performance of this FE, depicted in Fig. 7, is clearly influenced by the optimized bend, which is incorporated into the lower waveguide arm to decrease reflections.

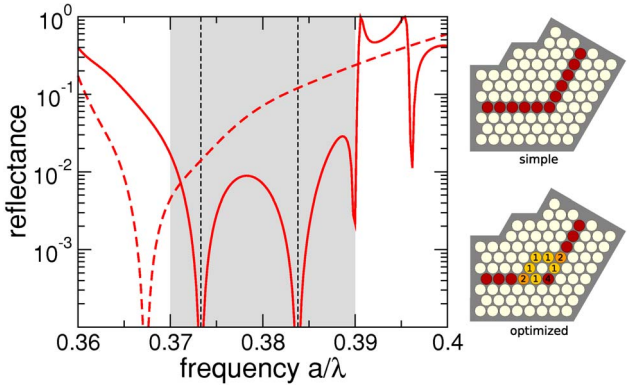

Fig. 6. (Color online) Reflectance of waveguide bends in the model system. The FE was optimized with respect to minimal total reflectance in the frequency range $a/\lambda=[0.370,0.390]$. A set of 3×3 pores was chosen, into which different low-index materials with refractive indices of $n=1.55$, 1.60, 1.65, and 1.70 were allowed to be infiltrated, indicated by numbers from 1 to 4 in the lower right panel, which depicts the optimized design. Only symmetric configurations with respect to a mirror reflection on the plane bisecting the angle enclosed by the bend were scanned. Consequently, the reflectance spectra of $(1+4)^6=15{,}625$ configurations were computed. The left panel shows the reflectance of the simple (dashed curve) and the optimized design (solid curve). The two vertical dashed lines mark the frequencies of minimal reflectance of the optimized design ($a/\lambda=0.373$ and 0.384). These lines are repeated in all the subsequent spectra in this paper.

C. Delay Line Transition

For an MZI circuit, it is necessary to introduce controlled phase shifts, e.g., to incorporate a delay line of a certain length into one arm. Such a delay line can be a slightly modified waveguide with a different dispersion relative to the reference waveguide in the second arm. As with the DC, we split the delay line into two congruent FEs: the transition to the delay line waveguide and the transition back. These are connected via a variable-length waveguide section. If the index change in the delay line waveguide relative to the reference waveguide is sufficiently weak, and the transitions are sufficiently smooth, the reflectance at the transitions is small enough for all frequencies of interest, so that the whole delay line can be approximately treated as an ideal phase shifter, albeit with modified dispersion, which accounts for the phase shifts relative to the MZI's second arm. In the MZI presented in Subsection 5.B, an index ratio of $n_{\text{delayline}}:n_{\text{ref}}=1.65:1.70$, and a transition region of two holes filled with materials of intermediate refractive index ($n=1.667$ and 1.683) is sufficient to reduce the reflectance at the delay line to less than 2% for all frequencies above $a/\lambda=0.368$. Nevertheless, in our computations, we treat the delay line transitions exactly, i.e., as full-fledged FEs on a par with bends and coupler end points.

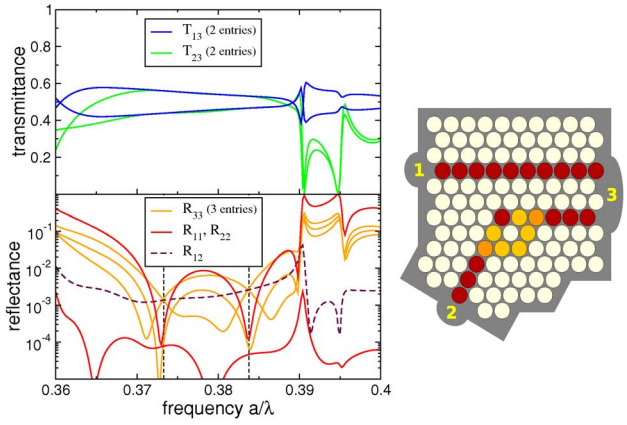

Fig. 7. (Color online) Coupler end point design (right panel) and its spectral performance (left panel). The FE consists of two single-mode waveguide ports (1 and 2) on the left and one dual-mode waveguide port (3) on the right. Undesirable reflectances have been reduced by utilizing the optimized design of the waveguide bend (see Fig. 6).

5. LARGE-SCALE PHOTONIC CRYSTAL CIRCUITS

The basic FEs described above may now be combined to construct more complex PhC-based circuitry. As an illustration, we design PhC-based DCs and MZIs, which could be useful in many WDM and sensing applications.

A. Directional Coupler

By combining two opposite coupler end points with a sufficiently long straight section between them (see Fig. 8), we can construct a DC of a certain length, i.e., a device consisting of two waveguides that come close to each other so that the fields can couple in a section of certain length.

The working principle of the DC is the following: in the coupling section, the two aligned single-mode waveguides form a dual-mode waveguide that supports an even and an odd propagating guided mode with respect to a certain symmetry of the system. In our case, this symmetry is a glide reflection, i.e., a reflection on the plane equidistant from both single-mode waveguides in combination with a translation of $a/2$ in the waveguide direction. These modes propagate with different wave vectors k_{even} and k_{odd}, respectively. Due to mode beating, the resulting field shifts periodically in space between the two single-mode waveguides with a period of $L_B=2\pi/|k_{\text{even}}-k_{\text{odd}}|$, called beat length. Thus, if the coupler length L is equal to L_B (or a multiple of it), light launched into one of the waveguides exits in the same waveguide (bar state), while if the coupler length is half the beat length (or an odd multiple of it), the light is completely coupled over to the other waveguide (cross state).

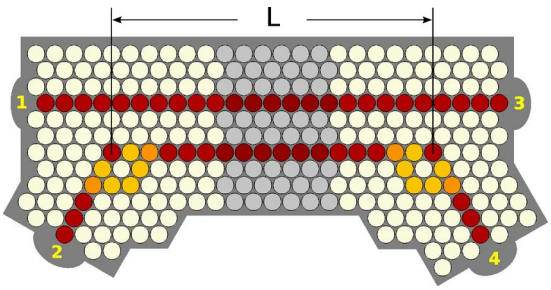

Fig. 8. (Color online) Directional coupler built into a PhC. It is decomposed into two coupler end points with a variable length waveguide between them (shaded region). Only the S-matrix of a single coupler end point and the (simple) switching matrix of the connecting dual-mode waveguide have to be computed for all frequencies of interest to allow design studies with couplers of any length.

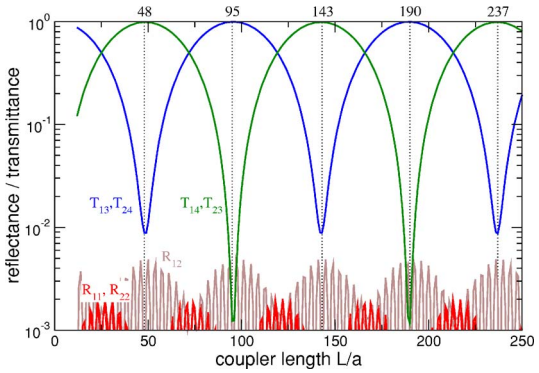

Fig. 9. (Color online) Length dependence of the reflectances and transmittances of the DC shown in Fig. 8 for a fixed frequency $a/\lambda = 0.373$.

Owing to the simple form of the switching matrix for this system, which only contains exponentials of the guided-modes' phase shifts over the length of the dual-mode waveguide, the entire design can be derived from only the guided modes of the single-mode and the dual-mode waveguide and the S-matrix of one coupler end point for all frequencies of interest. The length dependence of the DC for any frequency is then easily computed, since—for a given frequency—this only involves the combination of 4×4 S-matrices by means of Eq. (4).

Figure 9 shows the length-dependent performance of the DC for the fixed frequency $a/\lambda = 0.373$. The DC nicely shows the behavior described above. The "bar transmittance" T_{13} and the "cross transmittance" T_{14} alternate; the reflectances (including the "cross reflectance" R_{12}) are below 10^{-2}. There is a slight asymmetry between T_{13} and T_{14}, which stems from the asymmetry created by the bends in the lower coupler arm. From Fig. 9, we can estimate the beat length to be $L_B = 95a$. This is in very good agreement with the expected value of $L_B = 2\pi/|k_{\text{even}} - k_{\text{odd}}| = 94.1$ derived directly from dispersion data.

Due to the wavelength dependence of the beat length $L_B(\lambda)$, the frequency spectrum of the fixed-length DC (Fig. 10) shows an oscillating behavior of the transmittances in frequency regions where the reflectances ("backreflectances," R_{11} and R_{22}, as well as "cross reflectance", R_{12}) are small. In other regions the device performance is mainly governed by Fabry–Perot oscillations due to the nonnegligible reflectances and resonant behavior completely destroying the characteristic features of a DC. The frequency region of acceptable performance can be identified as $a/\lambda \in [0.368, 0.390]$.

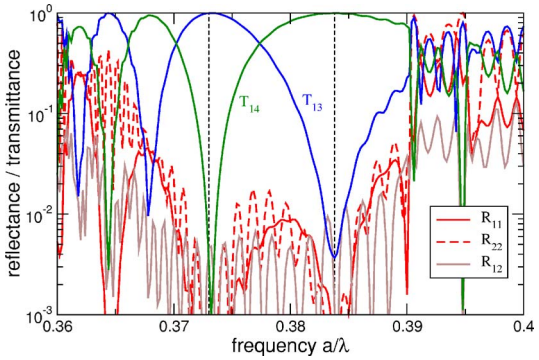

Fig. 10. (Color online) Reflectance/transmittance spectrum of a fixed-length DC as shown in Fig. 8 with $L = 97a$. For this length, the DC is in the bar state for $a/\lambda = 0.373$ and in the cross state for $a/\lambda = 0.384$.

B. Mach–Zehnder Interferometer

In the next step we combine two DCs by connecting them via two separate arms, see Fig. 11. We may incorporate a delay line into one arm by using a different low-index material ($n = 1.65$ instead of $n = 1.7$) to fill a certain number of pores in that arm. Such an MZI circuit can be the starting point for well-known wavelength flattening techniques to facilitate WDM applications [23,24].

To address this type of circuit, we require the S-matrices of the coupler end point, the waveguide bend, and the delay line transition described above. All these functional elements are small compared to the size of the entire circuit. Then, we are completely free to choose the two DC lengths L_1 and L_2 as well as the length of the MZI arms and the delay line length L_D.

First, we consider the balanced MZI with two equal arms. In Fig. 12 we display the performance of this circuit. It is apparent that such a balanced MZI is equivalent to a DC with effective length $L = L_1 + L_2$. This can be seen by comparing Figs. 10 and 12.

By incorporating a delay line into one arm, we can achieve an MZI with nonzero relative phase shifts $\Delta\phi$ between the waveguides in the two arms. The change of $\Delta\phi$ with frequency depends strongly on the length of the delay line and the index difference between the two arms. The delay line can be properly designed so that the phase shift is $2n\pi$, $n \in \mathbb{N}_0$ for one frequency ω_a and $(2n+1)\pi$ for a different frequency ω_b. The spectrum for this case is shown in Fig. 13. As compared to the balanced MZI (Fig.

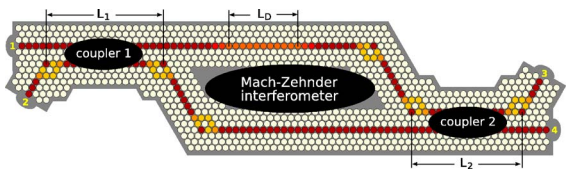

Fig. 11. (Color online) MZI consisting of two DCs of lengths L_1 and L_2 connected via two separate arms. In one arm a delay line of length L_D is realized by filling the pores with a different polymer with $n = 1.65$.

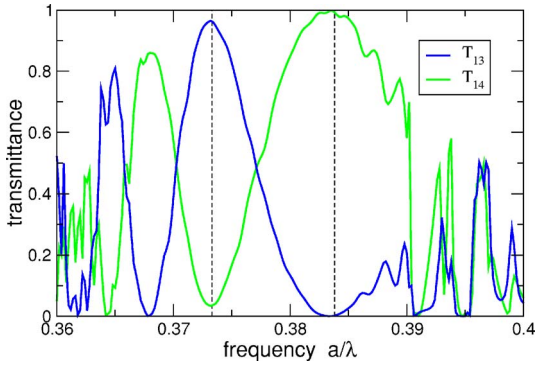

Fig. 12. (Color online) Spectrum of the MZI depicted in Fig. 11 with $L_1 = L_2 = 49a$ without a delay line (both arms have the same optical length). This balanced MZI acts as a DC of length $L_1 + L_2 = 98a$. Compare with Fig. 10.

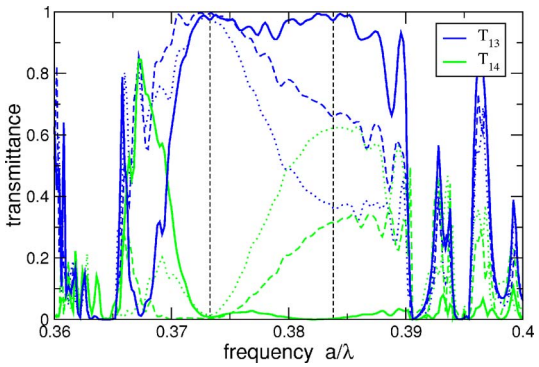

Fig. 13. (Color online) Spectrum of the MZI depicted in Fig. 11 with $L_1=L_2=49a$ and a delay line of variable length $L_D=17a$ (solid curves), $10a$ (dashed curves) and $6a$ (dotted curves). For $L_D=17a$, the relative phase shift approximately corresponds to $\Delta\phi=0$ at $a/\lambda=0.373$ and $\Delta\phi=\pi$ at $a/\lambda=0.384$. For shorter delay lines, it is still zero at $a/\lambda=0.373$, but takes some value $0<\Delta\phi<\pi$ at $a/\lambda=0.384$. Compare with the balanced MZI case ($\Delta\phi=0$ at all frequencies) in Fig. 12.

12), the MZI with delay line exhibits a large bar transmittance T_{13} at the frequency $a/\lambda=0.384$, while T_{13} is zero for that frequency in the balanced MZI. By using actively tunable materials such as liquid crystals or materials with intensity-dependent refractive index to create the delay line, this functionality can be used as a switch or modulator device.

6. SUMMARY

In this paper, we have introduced a Wannier-function based guided-mode S-matrix formalism for the design of complex PhC circuitry. We have applied the formalism to the realistic case of H-polarized light in macroporous silicon, where the FEs are created by single-pore infiltration with low-index materials (see [17] for the first experimental realization of such a system). By calculating S-matrices of small "basic" FEs, which act as building blocks, we can efficiently treat large and complex photonic circuits via an S-matrix combination. This approach scales much better than all-purpose techniques such as FDTD, and allows detailed design studies of large-scale circuits such as the directional coupler and MZI, which we have analyzed.

On the "lattice level" of PhCs, the Wannier function method allows efficient calculation and optimization of the S-matrices of basic FEs. It is capable of accurately treating the amplitude and phase of S-matrix entries. This is crucial for the correct treatment of circuits consisting of cascades of several basic FEs, such as MZI circuits. The efficiency of the Wannier-function approach in the reverse design of basic FEs has been demonstrated before [21,22], and in the present paper we have applied this approach to waveguide bends for H-polarized radiation in 2D macroporous silicon PhCs.

While the focus of the present paper has been on the design of large-scale devices, we would like to note that—to the best of our knowledge—this paper presents the first successful quantitative application of maximally localized photonic Wannier functions for H-polarized radiation in 2D PhCs. In addition, the extension of the Wannier-function based guided-mode S-matrix approach to 3D PhCs does not provide conceptual difficulties.

ACKNOWLEDGMENTS

We acknowledge the support of the Deutsche Forschungsgemeinschaft (DFG)-Forschungszentrum Center for Functional Nanostructures (CFN) at the University of Karlsruhe within project A1.1. The work of M. Schillinger was further supported by the German Academic Exchange Service (DAAD) through a one-year Ph.D. scholarship at the University of Central Florida, Orlando, Fla. In addition, we would like to acknowledge fruitful discussions with the members of the Deutsche Forschungsgemeinschaft–National Science Foundation (DFG–NSF) Materials World Project "Dynamic Photonic Crystals." Furthermore, we acknowledge discussions with Diederik Wiersma and Ralf Wehrspohn during the initiation of this project.

REFERENCES

1. K. Busch, G. von Freymann, S. Linden, S. F. Mingaleev, L. Tkeshelashvili, and M. Wegener, "Periodic nanostructures for photonics," Phys. Rep. **444**, 101–202 (2007).
2. A. Mekis, J. Chen, I. Kurland, S. Fan, P. R. Villeneuve, and J. Joannopoulos, "High transmission through sharp bends in photonic crystal waveguides," Phys. Rev. Lett. **77**, 3787–3790 (1996).
3. A. A. Green, E. Istrate, and E. H. Sargent, "Efficient design and optimization of photonic crystal waveguides and couplers: the interface diffraction method," Opt. Express **13**, 7304–7318 (2005).
4. A. Chutinan, M. Okano, and S. Noda, "Wider bandwidth with high transmission through waveguide bends in two-dimensional photonic crystal slabs," Appl. Phys. Lett. **80**, 1698–1700 (2002).
5. S. F. Mingaleev, M. Schillinger, D. Hermann, and K. Busch, "Tunable photonic crystal circuits: concepts and designs based on single-pore infiltration," Opt. Lett. **29**, 2858–2860 (2004).
6. M. Koshiba, "Wavelength division multiplexing and demultiplexing with photonic crystal waveguide couplers," J. Lightwave Technol. **19**, 1970–1975 (2001).
7. S.-H. Jeong, N. Yamamoto, J.-I. Sugisaka, M. Okano, and K. Komori, "GaAs-based two-dimensional photonic crystal slab ring resonator consisting of a directional coupler and bent waveguides," J. Opt. Soc. Am. B **24**, 1951–1959 (2007).
8. M. Soljacic, S. G. Johnson, S. Fan, M. Ibanescu, E. Ippen, and J. D. Joannopoulos, "Photonic-crystal slow-light enhancement of nonlinear phase sensitivity," J. Opt. Soc. Am. B **19**, 2052–2059 (2002).
9. K. Guven and E. Ozbay, "Coupling and phase analysis of cavity structures in two-dimensional photonic crystals," Phys. Rev. B **71**, 085108 (2005).
10. K. Busch and S. John, "Liquid crystal photonic band gap materials: the tunable electromagnetic vacuum," Phys. Rev. Lett. **83**, 967–970 (1999).
11. K. Yoshino, Y. Shimoda, Y. Kawagishi, K. Nakayama, and M. Ozaki, "Temperature tuning of the stop band in transmission spectra of liquid-crystal infiltrated synthetic opal as tunable photonic crystal," Appl. Phys. Lett. **75**, 932–934 (1999).
12. H. Takeda and K. Yoshino, "Tunable light propagation in Y-shaped waveguides in two-dimensional photonic crystals utilizing liquid crystals as linear defects," Phys. Rev. B **67**, 073106 (2003).
13. T. Yasuda, Y. Tsuji, and M. Koshiba, "Tunable light propagation in photonic crystal coupler filled with liquid crystal," IEEE Photon. Technol. Lett. **17**, 55–57 (2005).

14. S. F. Mingaleev and K. Busch, "Scattering matrix approach to large-scale photonic crystal circuits," Opt. Lett. **28**, 619–621 (2003).
15. K. Busch, S. F. Mingaleev, A. Garcia-Martin, M. Schillinger, and D. Hermann, "The Wannier function approach to photonic crystal circuits," J. Phys. Condens. Matter **15**, R1233–1256 (2003).
16. A. Birner, R. Wehrspohn, U. Gösele, and K. Busch, "Silicon-based photonic crystals," Adv. Mater. (Weinheim, Ger.) **13**, 377–388 (2001).
17. F. Intonti, S. Vignolini, V. Türck, M. Colocci, P. Bettotti, L. Pavesi, S. L. Schweizer, R. Wehrspohn, and D. Wiersma, "Rewritable photonic circuits," Appl. Phys. Lett. **89**, 211117 (2006).
18. K. Busch and S. John, "Photonic band gap formation in certain self-organizing systems," Phys. Rev. E **58**, 3896–3908 (1998).
19. H. Brand, *Schaltungslehre Linearer Mikrowellennetze* (Hirzel Verlag, 1970).
20. M. Schillinger, "Maximally localized photonic Wannier functions for the highly efficient description of integrated photonic crystal circuits," Ph.D. dissertation (University of Karlsruhe, 2006).
21. Y. Jiao, S. Fan, and D. Miller, "Demonstration of systematic photonic crystal device design and optimization by low-rank adjustments: an extremely compact mode separator," Opt. Lett. **30**, 141–143 (2005).
22. Y. Jiao, S. F. Mingaleev, M. Schillinger, D. Miller, S. Fan, and K. Busch, "Wannier basis design and optimization of a photonic crystal waveguide crossing," IEEE Photon. Technol. Lett. **17**, 1875–1877 (2005).
23. K. Jinguji, N. Takato, Y. Hida, T. Kitoh, and M. Kawachi, "Two-port optical wavelength circuits composed of cascaded Mach–Zehnder interferometers with point-symmetrical configurations," J. Lightwave Technol. **14**, 2301–2310 (1996).
24. M. Cherchi, "Design scheme for Mach–Zehnder interferometric coarse wavelength division multiplexing splitters and combiners," J. Opt. Soc. Am. B **23**, 1752–1756 (2006).